Prediction study of structural, thermal, and optical characterization of Co0.6Zn0.4Fe2O4 cubic spinel synthesized via sol–gel method for energy storage

Article *in* Journal- Korean Physical Society · May 2024

DOI: 10.1007/s40042-024-01078-8

Journal of the Korean Physical Society
https://doi.org/10.1007/s40042-024-01078-8

Online ISSN 1976-8524
Print ISSN 0374-4884

ORIGINAL PAPER - CONDENSED MATTER

Prediction study of structural, thermal, and optical characterization of $Co_{0.6}Zn_{0.4}Fe_2O_4$ cubic spinel synthesized via sol–gel method for energy storage

A. Messaoudi[1,2] · Aref Omri[2] · A. Benali[3,4] · M. A. Ghebouli[5,6] · A. Djemli[7,8] · M. Fatmi[5] · A. Habila[9] · Asma A. Alothman[9] · N. Hamdaoui[1] · R. Ajjel[10] · B. F. O. Costa[11] · M. F. P. Graca[4] · K. Khirouni[12]

Received: 4 March 2024 / Revised: 22 April 2024 / Accepted: 22 April 2024

Abstract

In this comprehensive study, we synthesized $Co_{0.6}Zn_{0.4}Fe_2O_4$ cubic spinel via the sol–gel method and characterized its structural, thermal, and optical properties. X-ray diffraction (XRD) verified the crystallization within the cubic Fd-3 m space group, and a detailed analysis determined a crystallite size ranging from 47 to 58 nm. Notably, the calculated crystallite size of 49.4 nm revealed inherent limitations in Scherer's formula, which does not account for intrinsic strain effects from crystal defects, grain boundaries, and stacking. Optical investigations, utilizing UV–Vis absorption spectroscopy, unveiled a direct optical band gap of 1.26 eV, suggesting semiconductor behavior. The material's thermal conductivity was found to be highly temperature sensitive, reaching its maximum value for both spin orientations at 900 K, with a quantified value of $ke/\tau = 4 \times 1014$ W/(mKs). This thermal behavior, along with the observed disorder (Eu value of 1.41 eV) and higher Urbach energy, offers valuable insights into the material's response under varying temperature conditions, essential for applications in diverse technological domains.

Keywords $Co_{0.6}Zn_{0.4}Fe_2O_4$ · Cubic spinel · Sol–gel synthesis · Semiconductor · X-ray diffraction · Crystallite size

✉ M. Fatmi
fatmimessaoud@yahoo.fr

[1] Laboratory of Energy and Materials (LabEM-LR11ES34), HigherSchool of Science and Technology of Hammam Sousse (ESSTHS), University of Sousse, Hammam, Sousse, Tunisia

[2] Laboratory of Advanced Multifunctional Materials and Technological Applications, Faculty of Science and Technology of Sidi Bouzid, University Campus Agricultural City, University of Kairouan, 9100 Sidi Bouzid, Tunisia

[3] Applied Physics Laboratory, Faculty of Sciences, University of Sfax, P.O. Box 1171, 3000 Sfax, Tunisia

[4] I3N and Physics Department, University of Aveiro, 3810-193 Aveiro, Portugal

[5] Research Unit on Emerging Materials (RUEM), University Ferhat Abbas of Setif 1, 19000 Setif, Algeria

[6] Department of Chemistry, Faculty of Sciences, University of Mohamed Boudiaf, 28000 M'sila, Algeria

[7] Faculty of Physics, University of Sciences and Technology Houari Boumediene (U.S.T.H.B), El Alia, Bab Ezzouar, BP 32, 16111 Algiers, Algeria

[8] Department of Physics, Faculty of Sciences, University of Mohamed Boudiaf, 28000 M'sila, Algeria

[9] Department of Chemistry, College of Science, King Saud University, P.O. Box 2455, 11451 Riyadh, Saudi Arabia

[10] Laboratory of Metabolic Biophysics and Applied Professional and Environmental Toxicology (LR12ES02), Faculty of Medicine Ibn El Jazzar, University of Sousse, 4002 Sousse, Tunisia

[11] CFisUC, Physics Department, University of Coimbra, Rua Larga, 3004-516 Coimbra, Portugal

[12] Laboratory of Materials Physics and Nanomaterials Applied to the Environment, Faculty of Sciences of Gabes, University of Gabes, Erriadh Campus, 6079 Gabes, Tunisia

Published online: 15 May 2024

1 Introduction

In recent years, there has been a lot of research on magnetic nanoparticles, especially nanoferrites, due to their many possible uses in different technical areas [1, 2]. The widespread production of nanoferrites is motivated by their exceptional characteristics, including unique structure, magnetic [3], and electrical properties [4], response to light, and thermal behavior [5]. These qualities make them suitable for various applications, such as magnetic sensors [6], MRI [7, 8], energy storage devices [9, 10], optoelectronics [11, 12], catalysis [13], and magnetic drug delivery [14, 15].

Spinel ferrite magnetic nanomaterials are especially interesting. They have a crystal structure similar to $MgAl_2O_4$, with a basic formula of AB_2O4. In this formula, 'B' is a trivalent cation like iron (Fe), and 'A' is a divalent cation which can be cobalt (Co), iron (Fe), nickel (Ni), zinc (Zn), manganese (Mn), tin (Sn), and others. These materials have been studied a lot because of their unique properties and belong to the space group Fd-3 m (Number 227 in international tables) [16–19].

Among different types of spinel ferrites, nanoferrites made of Co-$ZnFe_2O_4$ are very useful and interesting as magnetic materials. Specifically, cobalt ferrite ($CoFe_2O_4$) is very promising for several uses. These include delivering drugs with magnets, making high-quality audio and video tapes [20], optical discs [21], and digital records [22]. This is because of its strong magneto crystalline anisotropy [23], which means it has a strong preferred direction of magnetism [24] and great chemical and physical stability [25]. The magnetic characteristics of $CoFe_2O_4$ can be significantly changed by adding the right amount of non-magnetic (diamagnetic) impurities [26, 27]. There are many ways to synthesize Co-$ZnFe_2O_4$ nanoferrites, like the solid-state reaction method, or ceramic method [28], microwave combustion [29], forced hydrolysis [30], co-precipitation [31], and the sol–gel method [32, 33]. The sol–gel method, which is also called a solution-burning technique, has been particularly useful for making spinel ferrite nanoparticles in the last 20 years. This method has been used to create a wide variety of spinel ferrite materials [32, 33].$Co_xZn_{1-x}Fe_2O_4$ nanoferrites, especially those with zinc (Zn) replacing some of the cobalt (Co), are getting a lot of attention because they have better magnetic and electrical properties [34–37]. These ferrites have many good features like a large surface area, strong magnetization, high magnetic permeability, a big dielectric constant, high electrical resistance, good chemical stability, and low dielectric loss. These qualities make them great for electronic devices that work at high frequencies [36–38]. $CoFe_2O_4$ is a type of ferrite where Co^{2+} ions are in octahedral positions and Fe^{3+} ions are in both octahedral and tetrahedral positions. Adding non-magnetic Zn^{2+} cations, which take the place of some Fe^{3+} cations at the tetrahedral sites, is thought to increase the magnetization without much change to the electrical properties [36–40].

This study provides a comprehensive examination of the $Co_{0.6}Zn_{0.4}Fe_2O_4$ cubic spinel synthesized through the sol–gel method, focusing on its structural, thermal, and optical properties. Our findings, supported by X-ray diffraction and UV–Vis absorption spectroscopy, have confirmed the material's semiconducting nature and its potential for high-tech applications. The observed temperature-sensitive thermal conductivity. These results not only deepen our understanding of the $Co_{0.6}Zn_{0.4}Fe_2O_4$ cubic spinel's multifaceted properties but also highlight its promising utility in areas requiring materials with specific thermal and optical characteristics. The insights gained from this study pave the way for future research and development of similar materials, potentially leading to innovative applications in various advanced technological fields.

2 Experimental details

2.1 Preparation of $Co_{0.6}Zn_{0.4}Fe_2O_4$ ferrite

The synthesis of $Co_{0.6}Zn_{0.4}Fe_2O_4$ spinel ferrite was achieved through the sol–gel method, a technique chosen for its numerous advantages including enhanced uniformity, reduced processing temperatures, shorter annealing durations, elevated purity, and superior material characteristics. This method was effectively utilized to generate high-quality materials. For the synthesis, reagent-grade metal nitrates $Fe(NO_3)_2{\cdot}9H_2O$, $Zn(NO_3)_2{\cdot}6H_2O$, and $Co(NO_3)_2.4H_2O$, all procured from Sigma-Aldrich with purity levels of 99.9%, 98%, and 99.9%, respectively, were used along with ethylene glycol ($C_2H_6O_2$, 99%).

In the meticulous preparation of $Co_{0.6}Zn_{0.4}Fe_2O_4$ nanoferrite via the sol–gel technique, specific stoichiometric ratios of zinc, copper, and iron nitrates were precisely measured and dissolved in distilled water. The solution was then heated at 90 °C with constant stirring in a fume hood to initiate the formation of a sol. Citric acid, added in a 1:3 molar ratio to the metal nitrates, served as a chelating and combustion agent, while ethylene glycol was included as a polymerization catalyst. This mixture was stirred and heated for 2 h until a dense, dark gel formed. This gel was dried at 200 °C to create a xerogel. The xerogel was then calcined at 400 °C for 24 h to ensure complete decomposition of the precursor and formation of the desired $Co_{0.6}Zn_{0.4}Fe_2O_4$ phase.

The calcination process continued with the powder being crushed and calcined at 600 °C for 24 h, ground once more, and then calcined again at 700 °C for 24 h. The granular

material was then compacted into pellets using a high-pressure ten ton/cm^{2}press, creating pellets with a 1 mm thickness and a 10 mm diameter. These pellets were sintered at 1000 °C for 24 h to achieve the desired crystalline phase of the nanoferrite. For the final stage, the resulting pellets were carefully ground and pelletized again, followed by another grinding step. The material was then sintered for 12 h at 1000 °C. This comprehensive process, which includes multiple grinding, pelletizing, and calcination steps, ensures the development of a well-structured ferrite product. Throughout these procedures, the sample was subjected to standard laboratory conditions, maintaining an ambient temperature of approximately 25 °C (77 degrees Fahrenheit) and a pressure of 1 atmosphere. This comprehensive process, which includes multiple grinding, pelletizing, and calcination steps, ensures the development of a well-structured ferrite product while adhering to standard laboratory conditions during the heating and calcination stages. In the final stage of the process, the resulting pellets were meticulously ground and pelletized again. The grinding was conducted manually using a mortar and pestle to ensure a controlled and precise reduction in pellet size, maintaining the integrity of the material while achieving the desired characteristics, rather than by ball milling which could introduce contamination or damage the material. This manual grinding approach allowed for a careful breakdown of the pellets into a finely powdered form suitable for characterization, while avoiding potential issues from mechanized grinding methods. The structural and compositional attributes of the final product were then characterized through advanced analytical methods, including XRD, SEM, and Raman spectroscopy, to confirm the successful synthesis of the $Co_{0.6}Zn_{0.4}Fe_2O_4$ nanoferrite with the desired properties.

2.2 Characterization techniques

For XRD analysis, a minimal amount of material, approximately 0.2 g, was finely powdered and uniformly dispersed on the sample holder. The XRD pattern was collected at room temperature over a 2θ range of 10°–80° employing a Bruker 8D Advance X-ray powder diffractometer, equipped with monochromatized Cu-Kα radiation (wavelength λ = 1.5406 Å).

Calibrating X-ray diffraction (XRD) equipment involves crucial steps to ensure accuracy. Starting with a standard sample, we optimize instrument parameters, align the sample holder, and calibrate the zero angle. Lattice parameter refinement is performed, and peak profile fitting techniques are employed for precise analysis. Regular calibration checks using certified reference materials are essential to maintain the accuracy of XRD measurements over time. These steps collectively establish a well-calibrated instrument, enhancing the reliability of subsequent crystalline material analyses. Rietveld refinement was employed to optimize the XRD data, utilizing the Fullprof tool for determining cell parameters, phase purity, and homogeneity of the synthesized sample. The material's morphology was examined using a TESCAN VEGA3 SBH scanning electron microscope (SEM) with a BurkerXFlagh 410 M EDS detector.

Several spectroscopic techniques were performed to investigate the properties of the product. Raman spectroscopy, using a Raman microsystem (HoribaLabRam HR Evolution) with an excitation wavelength of 532 nm, an open-space confocal microscope, a CCD detector, and a 600 gmm^{-1} grating, was utilized to determine the spinel structure and study its vibrational motions. For analyzing the optical properties, UV–Vis spectra were acquired at room temperature with a UV3101PC scanning spectrophotometer, covering a wavelength range of 200 to 2400 nm. Absorbance (A) and reflectance (R) were calculated based on these measurements.

3 Results and discussion

3.1 Structural properties

Figure 1 displays the Rietveld X-ray diffraction (XRD) pattern of the $Co_{0.6}Zn_{0.4}Fe_2O_4$ refined powder sample using the Fullprof software. The pattern shows the (111), (220), (311), (222), (400), (422), (511), (440), (531), (620), (533), and (622) lattice planes, confirming the formation of a single-phase spinel structure with the Fd-3 m space group. The Bragg peak profile was described using the pseudo-Voigt function. No additional reflections were observed at Bragg

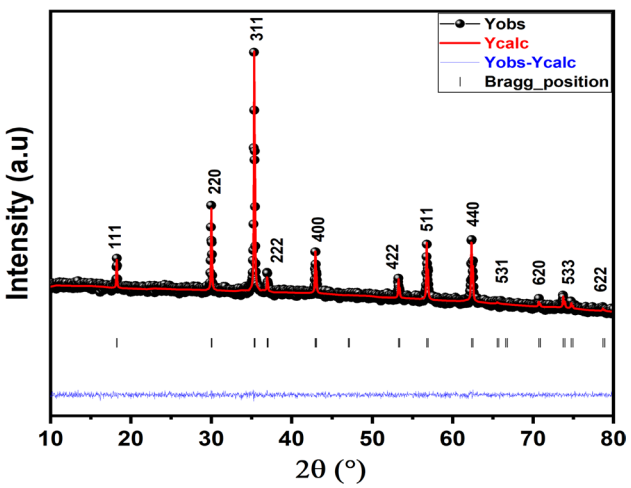

Fig. 1 XRD pattern with Rietveld refinement for $Co_{0.6}Zn_{0.4}Fe_2O_4$. The underneath line (blue) depicts the difference between the XRD data (black) and calculated fit (red), and the green lines are Bragg positions

peak positions corresponding to any other phase than the spinel ferrite, as demonstrated in the diffraction pattern [41]. Furthermore, the standard JCPDS card number 22-1086 of the pure cobalt spinel ferrite structure $CoFe_2O_4$ and the indexed Miller indices for diffraction peaks are in good agreement [42]. The peak broadening in the XRD pattern is explained by the nanoscale dimensions of the crystallites.

For the spinel phase, the precise determination of the cation distribution within the tetrahedral (A) and octahedral [B] sites is essential for the Rietveld refinement of the XRD patterns of $Co_{0.6}Zn_{0.4}Fe_2O_4$ compounds. Mössbauer spectroscopy has been employed to estimate the cation positions for ferrite samples with the chemical composition AB_2O_4. Previous studies, utilizing Mössbauer spectroscopy, have revealed that in certain ferrites containing (Co, Zn, and Fe), Zn^{2+} ions tend to occupy the A sites preferentially. Conversely, Co^{2+} ions are distributed across the B sites, while Fe^{3+} ions can be found at both sites [43, 44]. As a result, the cation distribution for the $Co_{0.6}Zn_{0.4}Fe_2O_4$ sample can be expressed as $\left(Zn_{0.4}^{2+}Fe_{0.6}^{3+}\right)_A\left[Co_{1.4}^{2+}Fe_{0.6}^{3+}\right]_B O_4^{2-}$. The positions for [B] cations, (A) cations, and O were taken in the Rietveld refinement at positions 16d (1/2,1/2,1/2), 8a (1/8,1/8,1/8), and 32e (x, y, z), respectively.

Furthermore, the broadening of the XRD pattern's lines hints at the nanoscale dimensions of the crystallites within the sample. Such broadening is often indicative of small particle sizes, which lead to an increase in the line width due to the X-ray diffraction size effect. The Rietveld refinement process not only confirms the phase purity and structure but also yields vital quantitative data about the sample.

The mean crystallite size was initially estimated using the standard Scherer method, which entails using the Scherer formula presented in Eq. (6) [45–51]:

$$D_{SC} = \frac{k\lambda}{\beta\cos\theta}, \tag{1}$$

where k is a constant ($k = 0.89$), λ the wavelength of the X-ray radiation, β the full width at half maximum of the most intense peak (311) (FWHM) given in radians, and θ is the diffraction angle. The average crystallite size in our sample is 47.4 nm. To mitigate potential sources of error during the calculation of the typical size of a crystallite, we employ the adapted Scherer equation (Eq. 2) [52]:

$$\ln\beta = \ln\frac{k\lambda}{D_{sc}} + \ln\frac{1}{\cos\theta}. \tag{2}$$

In Fig. 2a, the plot of $\ln\beta$ as a function of $\ln(1/\cos\theta)$ enables the determination of the average crystallite size by calculating the intercept of the linear fit. Using this method, the calculated crystallite size is 49.4 nm. However, Scherer's formula does not consider the effect of intrinsic strain resulting from crystal defects, grain boundaries, and stacking [41, 53]. To account

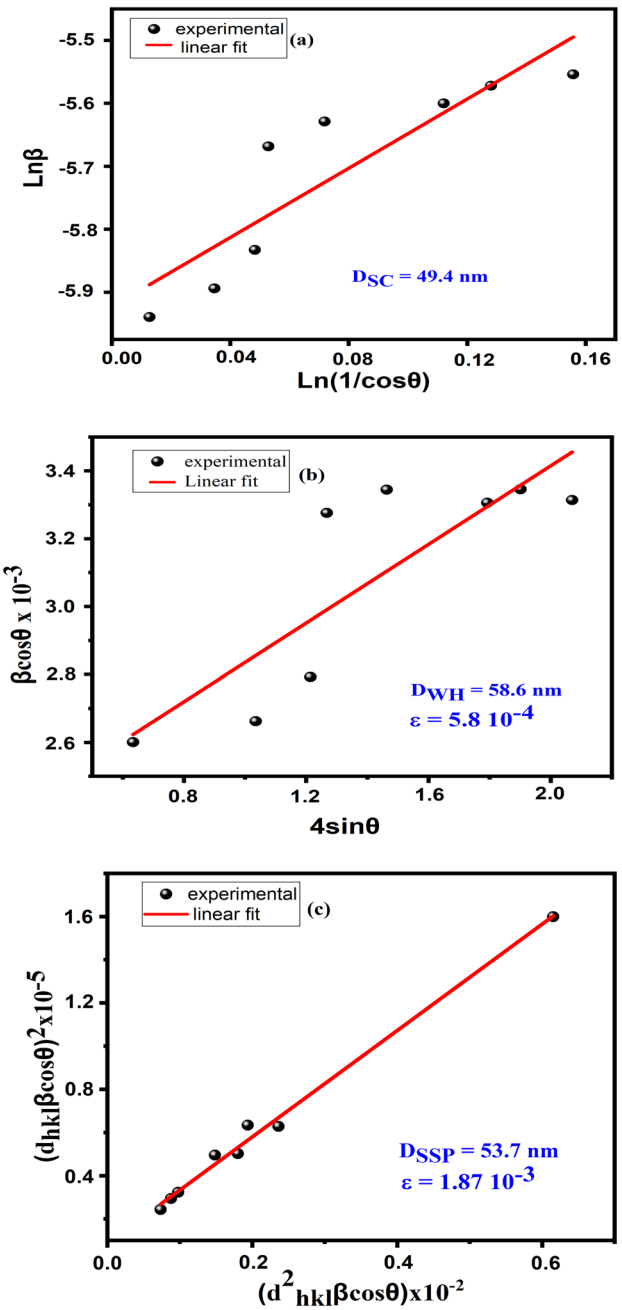

Fig. 2 Modified Scherer graph (**a**), Williamson–Hall graph (**b**), and size–strain graph (**c**) for $Co_{0.6}Zn_{0.4}Fe_2O_4$

for the intrinsic strain, the Williamson–Hall (W–H) approach can be used to estimate the crystallite size and also consider the strain-induced broadening of XRD peaks [54, 55]. The calculation of intrinsic strain is achieved by applying Eq. (3) below [56]:

$$\beta\cos\theta = \frac{k\lambda}{D_{WH}} + 4\varepsilon\sin\theta, \tag{3}$$

where ε is the strain. Figure 2b depicts the plotting of this Eq. (3), with the term (4sin θ) along the abscissa axis and (β_{hkl}.cos θ) along the ordinate axis. The crystallite size of the $Co_{0.6}Zn_{0.4}Fe_2O_4$ ferrite can be deduced from the intercept value of the linear curve, while its slope provides the fundamental strain value. The obtained values of D_{WH} and ϵ are, respectively, 58.6 nm and 5.8×10^{-4}.The technique known as size–strain plot (SSP) interprets the XRD peak profile as a combination of Gaussian and Lorentzian functions, where the Lorentzian function represents the broadening of the XRD curve and the Gaussian function represents the stretching [53]. Equation (9) is used to calculate the SSP, as shown below [57].

$$\left(d_{hkl}\beta\cos\theta\right)^2 = \frac{k\lambda}{D}\left(d_{hkl}^2\beta\cos\theta\right) + \frac{\varepsilon^2}{4}. \quad (4)$$

As illustrated in Fig. 2c, a graph is produced using Eq. (4), with the terms $\left(d_{hkl}^2\beta\cos\theta\right)$ along the abscissa axis and $(d_{hkl}.\beta.\cos\theta)^2$ along the ordinate axis. The slope of the linear fit results in an average D_{SSP} of 53.7 nm, and the intrinsic strain estimated from the intercept was 1.87×10^{-3}. Table 1 summarizes the findings of the average crystallite size and strain values calculated using the various methods.

3.2 Elemental and morphological analysis

The fracture microstructure image of $Co_{0.6}Zn_{0.4}Fe_2O_4$ ferrite was analyzed by scanning electron microscope (SEM). The SEM illustration and agglomeration of grains distribution of our sample are shown in Fig. 3. The SEM image clearly illustrates the distinct chemical contrast of the ferrite phase. In addition, it displays the non-uniform surface behavior of the regularly shaped agglomeration of grains, which exhibit large facets. The presence of black dots indicates the porosity of the sample. Moreover, the SEM image of the investigated compound closely resembles those of pure or doped spinel ferrite systems prepared using other methods such as solid-state, autocombustion, co-precipitation, and microwave irradiation methods. In previous studies, researchers have observed large agglomerates with small particles adhering to their surfaces, similar to what is observed in our SEM image [58–60]. The EDS spectrum exhibits distinct peak intensities corresponding to Co, Zn, Fe, and O elements, providing evidence of their presence. The dominant elements identified in the sample include oxygen (25.80%), iron (36.63%), cobalt (10.97%), and zinc (7.68%). The percentage composition values obtained from the EDS analysis offer quantitative insights into the relative abundance of each element. Iron emerges as a significant component, constituting the highest percentage among the identified elements. Cobalt and zinc also contribute noticeably to the overall composition, confirming their presence in the material. Oxygen, as expected, constitutes a substantial proportion, reflecting the oxides and compounds in the sample.

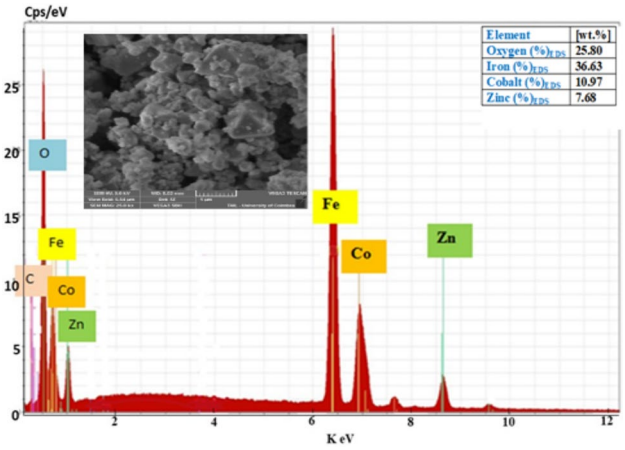

Fig. 3 SEM image and EDS spectrum for $Co_{0.6}Zn_{0.4}Fe_2O_4$ ferrite

3.3 Raman spectroscopy

The findings from group theory analysis propose that the cubic configuration exhibits ten active Raman modes, out of which five ($A_1g + Eg + 3T_2g$) are linked to the movement of oxygen ions at one or both A and B sites [61, 62]. In this study, Raman spectra were obtained at room temperature for $Co_{0.6}Zn_{0.4}Fe_2O_4$ in the 150–800 cm^{-1} range. In our Raman spectral analysis, we meticulously performed background extraction following established procedures. This involved systematic steps such as baseline correction to eliminate instrumental effects, polynomial fitting to model and subtract background signals, and an iterative process for optimal adjustment of parameters. Visual inspection was crucial to confirm the effectiveness of background subtraction, addressing any residual signals or artifacts. By employing these techniques, we

Table 1 Crystallite size and strain values obtained using several methods

Method	Crystallite size	Strain
Scherrer method	$D_{SC}=47.4\ \text{nm}\pm2.1\ \text{nm}$	–
Modified Scherrer method	$D_{SC}=49.4\ \text{nm}\pm2.2\ \text{nm}$	–
Williamson–Hall method	$D_{WH}=58.6\ \text{nm}\pm0.6\ \text{nm}$	$\varepsilon=5.8\times10^{-4}\pm3\times10^{-5}$
Size–strain plot method	$D_{SSP}=53.7\ \text{nm}\pm0.6\ \text{nm}$	$\varepsilon=1.87\times10^{-3}\pm3\times10^{-5}$

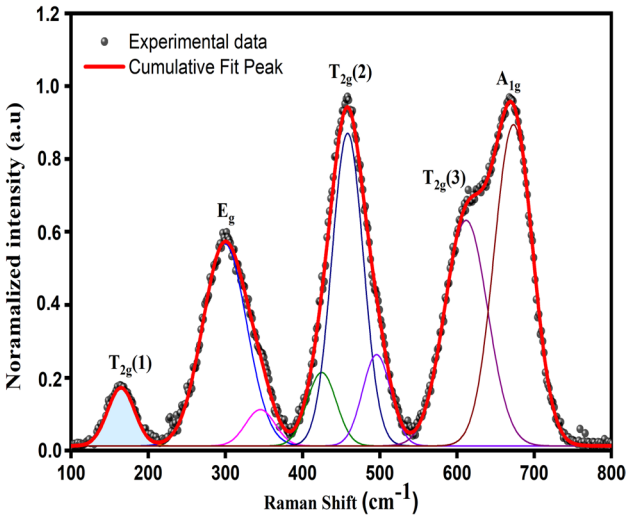

Fig. 4 Room temperature Raman spectrum for $Co_{0.6}Zn_{0.4}Fe_2O_4$ ferrite spinel

ensured accurate and reliable Raman spectral analysis, enhancing peak visibility and improving the signal-to-noise ratio. The Raman spectrum of the sample under investigation indicates five Raman bands associated with the Zn and Co spinel ferrite materials of space group Fd-3 m [63–66]. These observations are consistent with the structural analysis of the compound reported earlier. The Raman spectrum of the studied compound was analyzed by fitting it with a Lorentzian line shape and deconvolving it into eight peaks, as shown in Fig. 4. The peak observed at 669 cm^{-1} is attributed to the A_1g mode, which is related to the bond stretching vibrations of (Fe/Co/Zn)-O and metal–oxygen in the tetrahedral sites.

The peaks observed at frequencies around 165, 301, 458, and 609 cm^{-1} were assigned to the T_{2g} and E_g modes, which correspond to the vibration of the spinel structure [65]. Notably, the relative intensity and area of the $T_2g(3)$ and $T_2g(2)$ peaks were higher than those reported in previous studies [67, 68], indicating the effect of 40% Co^{2+} ion substitution by Zn^{2+} ions on the distribution of cations between octahedral and tetrahedral sites. Two additional peaks were detected at around 420 and 500 cm^{-1}, resulting from the splitting of the Raman $T_2g(2)$ mode, which is related to the site of the octahedral sublattice as reported by Dattet al. [68]. This confirms that the octahedral spinel ferrite site contains Zn^{2+}, Co^{2+}, and Fe^{3+} ions. Lastly, the peak observed at approximately 350 cm^{-1} was previously reported to be related to the symmetrical bending of oxygen with respect to the cations and the translational motion of the entire cation-O_4 tetrahedron [65].

3.4 Optical properties

Optics measurements play a crucial role in assessing a compound's luminous efficiency and overall quality. Various optical properties, such as gap energy, absorption coefficient, Urbach energy, extinction coefficient, and penetration depth, are determined through absorption spectroscopy. In Fig. 5, we present the absorption spectrum (λ) of sample A, recorded at ambient temperature within the wavelength range of 200–2400 nm. In addition, the inset of the same figure displays the reflectance spectrum R(λ). Notably, the compound exhibits remarkable light absorption behavior, particularly in the ultraviolet and visible light ranges. To quantify the optical absorption coefficient, we employ the Beer–Lambert Eq. (10), leveraging the data obtained from the absorption spectrum [69]:

$$a = \frac{2.303 \times A}{d}, \tag{5}$$

where A and d represent the absorbance and thickness of the sample, respectively.

The optical band gap (Eg) can be determined directly from the minimum of (dα/dλ), derivative from α with respect to λ [70]. The curves α and dα/dλ as functions of λ are plotted in Fig. 6.

The band gap energy is then obtained by the following formula Eq. (6):

$$E_g = \frac{hC}{\lambda}, \tag{6}$$

where c and h are, respectively, the speed of light and Planck's constant.

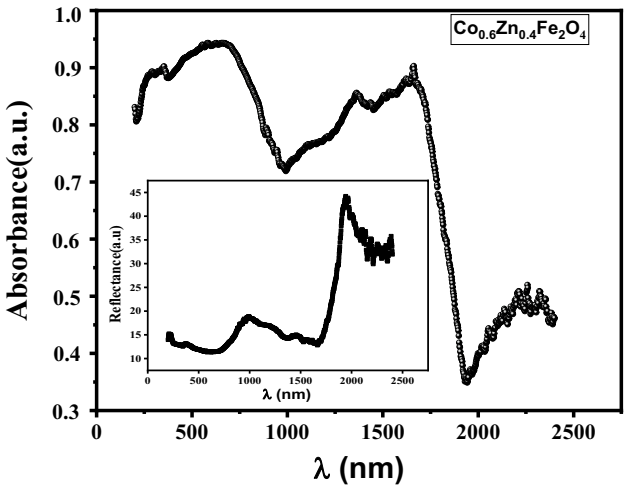

Fig. 5 UV–Vis absorbance spectrum A(λ) for $Co_{0.6}Zn_{0.4}Fe_2O_4$ferrite spinel. Inset: reflectance spectrum R(λ)

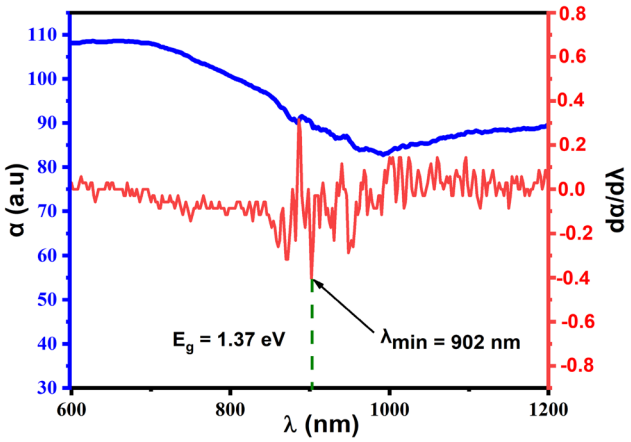

Fig. 6 Variations of the coefficient (α) and its derivative (dα/dλ) versus λ for $Co_{0.6}Zn_{0.4}Fe_2O_4$ ferrite spinel

From the minimum value of the dα/dλ curve, we estimate the value of $\lambda_{min} = 902$ nm, which then gives a band gap energy of $E_g = 1.37$ eV. The value of E_g can be more accurately calculated using Tauc's law Eq. (7) [71]:

$$(ah\vartheta)^{1/n} = \beta\left(h\vartheta - E_g\right), \tag{7}$$

where β is a parameter that describes the degree of disorder in the compound, α is the absorption coefficient, E_g is the width of the forbidden band, hυ is the incident radiation energy expressed in eV, and the exponent n describes the nature of the optical transition: $n = 1/2$ for an authorized direct transition and $n = 2$ for an authorized indirect band gap [72].

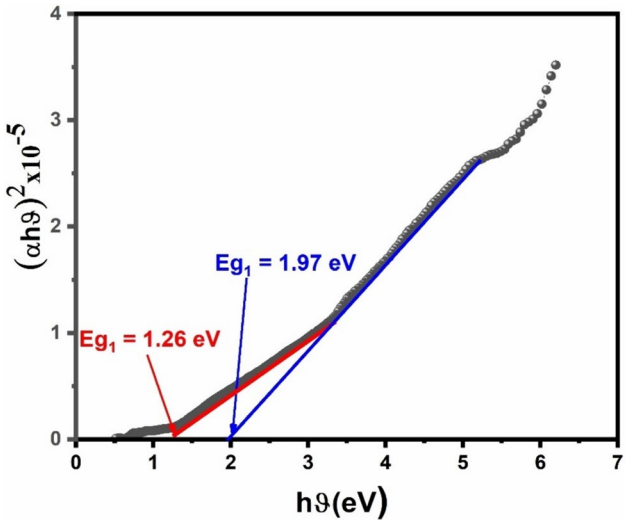

Fig. 7 Curve of $(\alpha h\nu)^2$ as a function of hν for $Co_{0.6}Zn_{0.4}Fe_2O_4$ ferrite spinel

Figure 7 illustrates the curve of $(\alpha h\vartheta)^2$ as a function of hϑ for the direct transition in the $Co_{0.6}Zn_{0.4}Fe_2O_4$ sample. Notably, two linear extrapolations are employed to determine distinct band gap energies. The first extrapolation, yielding $E_{g1} = 1.26$ eV, involves the linear section of the spectrum at $h\vartheta = 0$, consistent with our prior calculation based on the dα/dλ curve. This value aligns with the charge transfer processes denoted by E_{g1}, involving Fe^{3+} (π^*t_2) and Fe^{2+} (σ^*t_2) or Co^{3+} (π^*t_2) and Co^{2+} (σ^*t_2), indicating an internal oxidation–reduction process within the unit cell. In addition, a second linear extrapolation at $h\vartheta = 0$ determines $E_{g2} = 1.97$ eV, corresponding to E_{g2} and representing charge transfer between $Co^{2+}(\pi_T)$ and $Fe^{3+}(\sigma^*t_2)$. This value signifies the actual bandgap of Zn-doped $CoFe_2O_4$, associated with interband transitions [73–76, 76]. The identification of two distinct bandgap values through these extrapolations enhances the precision of our analysis and underscores the material's potential for diverse applications, given its favorable electronic properties [77].

Using the following Eq. 8, we can verify the kind of optical transition:

$$\ln(ah\vartheta) = \ln\beta + n\ln\left(h\vartheta - E_g\right). \tag{8}$$

We draw $\mathrm{Ln}(ah\vartheta)$ as a function of $\mathrm{Ln}(h\vartheta - E_g)$ using the previous E_g value ($E_{g1} = 1.26$ eV), as shown in Fig. 8. The slope of the linear fit of the curve yields n on the verge of 0.5, confirming the direct transition for our compound.

The Urbach energy Eu, which corresponds to the transition between the extended state of the valence band and the confined state of the conduction band, is an essential characteristic for distinguishing material disorder [77, 78]. In theory, the Urbach energy Eu may be calculated using the Urbach-Martienssen model Eq. (9):

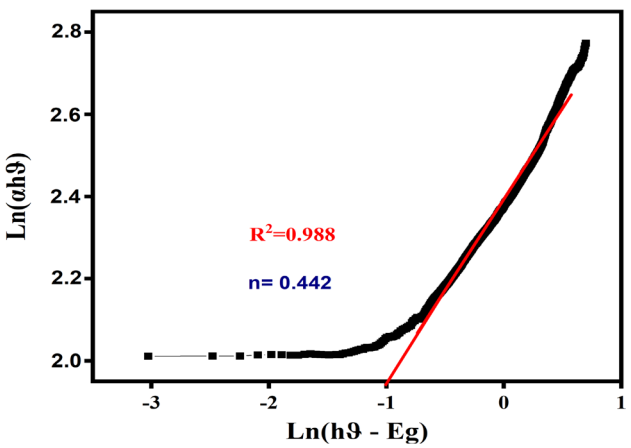

Fig. 8 Plot of Ln(αhυ) as a function of Ln $(h\vartheta - E_g)$ for $Co_{0.6}Zn_{0.4}Fe_2O_4$ ferrite spinel

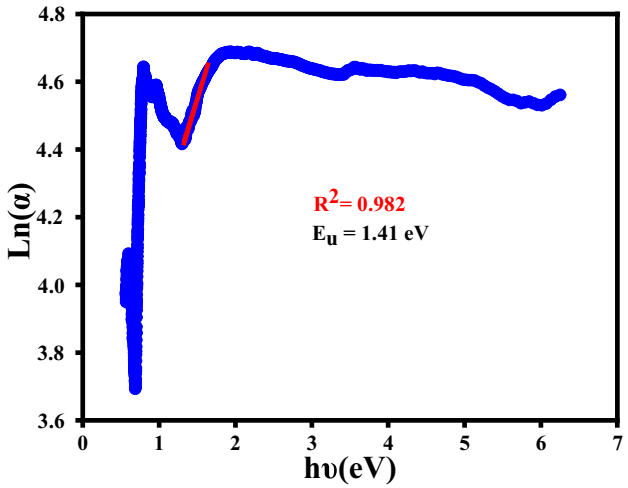

Fig. 9 Plot of Ln(α) as a function of hυ for $Co_{0.6}Zn_{0.4}Fe_2O_4$ ferrite spinel

$$a = a_0 \exp\left(\frac{h\vartheta - E_g}{E_u}\right), \tag{9}$$

where a_0 is a constant and E_u is the Urbach energy.

Taking the logarithm of the above, we get the following relation Eq. 10:

$$\ln a = \ln a_0 \left(\frac{h\vartheta - E_g}{E_u}\right). \tag{10}$$

Using this relationship, the Urbach energy E_u may be calculated from the slope of the linear component of the curve Ln(α) as a function of hυ as illustrated in Fig. 9. The observed E_u value of 1.41 eV demonstrates the presence of a massive disorder in the produced material. Furthermore, the larger value of the Urbach energy represents the higher density of localized states in the composite [79]. The absorption of electromagnetic radiation by a material is influenced by various factors, such as the penetration depth (δ) and the extinction coefficient (k). The penetration depth (δ) describes the attenuation of the incident wave within the material and is defined as the depth at which the intensity of the incident beam is decreased to 1/e of its initial value at the surface [80]. This can be expressed mathematically using the following Eq. 11:

$$\delta = \frac{1}{a}, \tag{11}$$

The extinction coefficient (k) quantifies the reduction of the electromagnetic wave in the medium [81]. It is provided via the following Eq. 12:

$$k = \frac{a\lambda}{2\pi}. \tag{12}$$

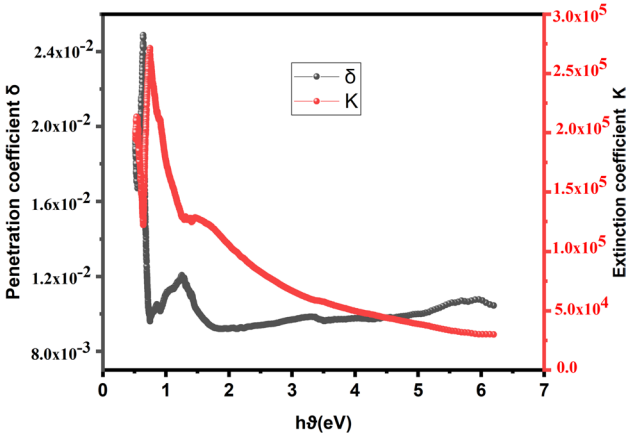

Fig. 10 Variations of the penetration depth (δ) and optical extinction (k) as a function of hν for $Co_{0.6}Zn_{0.4}Fe_2O_4$ ferrite spinel

The graphical analysis presented in Fig. 10 provides valuable insights into the behavior of δ and k in relation to photon energy ($h\upsilon$). The observed trends reveal two distinct regions, marked by noteworthy peaks in both δ and k when photon energy approaches 1 eV. This phenomenon is intelligibly linked to heightened surface absorption, enabling effective light penetration and information retrieval at increased depths within the material.

Conversely, beyond the 1 eV threshold, the graph depicts a decline in both coefficients with rising hυ. This diminishing trend is attributed to the decreasing photon energy within the surface region, resulting in intensified absorption and hindering the light's ability to detect the lower interface of the layer of particular significance is the clear indication that the "information depth" significantly surpasses the "penetration depth," as calculated by λ/(4πk). This discrepancy is accentuated by the sustained low uncertainty observed at a wavelength of 450 nm. Despite the optical penetration depth (OPD) predicting an approximate value of 240,000 nm, the measured layer thickness is around 2,000,000 nm [82–86]. This incongruity underscores the intricate interplay between optical properties and layer characteristics, emphasizing the imperative need for a nuanced understanding of the material's behavior under varying photon energies.

4 Conclusion

In this study, we have thoroughly investigated the structural, vibrational, and optical characteristics of $Co_{0.6}Zn_{0.4}Fe_2O_4$ cubic spinel synthesized via the sol–gel method. The XRD studies confirmed the nanograin-sized cubic Fd-3 m structure. While the calculated crystallite size is 49.4 nm, it is crucial to note that Scherer's formula does not consider intrinsic strain effects from crystal defects, grain boundaries,

and stacking. The observed Eu value of 1.41 eV indicates significant disorder, and the larger Urbach energy highlights a higher density of localized states in the composite. These findings deepen our understanding of the material's properties and underscore the complex nature of $Co_{0.6}Zn_{0.4}Fe_2O_4$, offering potential avenues for diverse technological applications. Moreover, our investigation into the optical band gap, determined to be 1.26 eV, aligns with semiconductor behavior, showcasing the material's potential suitability for specific applications. The thermal conductivity study revealed sensitivity to temperature variations, with the peak thermal conductivity observed at 900 K for both spin types. Notably, an increase in chemical potential led to a rise in the total thermal conductivity.

Acknowledgements This work was supported by the Tunisian Ministry of Higher Education and Scientific Research with the collaboration of national funds from FCT – Fundação para a Ciência e a Tecnologia, I.P., within the project UID/04564/2020. Access to TAIL-UC facility funded under QREN-Mais Centro Project No. ICT_2009_02_012_1890 is gratefully acknowledged.

Funding This work was funded by the Researchers Supporting Project Number (RSP2024R243) at King Saud University, Riyadh, Saudi Arabia.

Data availability Not applicable.

Declarations

Conflict of interest The authors declared no potential conflicts of interest with respect to the research, authorship, and/or publication of this article.

References

1. S. Hazra, N. Ghosh, Preparation of nano ferrites and their applications. J. Nanosci. Nanotechnol. **14**, 1983–2000 (2014)
2. I. F. Cruz, C. Freire, J. P. Araújo, C. Pereira and A. M. Pereira, Multifunctional ferrite nanoparticles: from current trends toward the future. *Magnetic nanostructured materials* (Elsevier) 59–116 (2018)
3. S. Sharma, K. Daya, S. Sharma, M. Singh, Ultra low loss soft magnetic nanoparticles for applications up to S-band. Appl. Phys. Lett. **103**, 35 (2013)
4. G. Aravind, D. Ravinder, V. Nathanial, Structural and electrical properties of Li–Ni nanoferrites synthesised by citrate gel autocombustion method. Phys. Res. Int. (2014). https://doi.org/10.1155/2014/672739
5. J.A. Vara, P.N. Dave, S. Chaturvedi, The catalytic investigation of nanoferrites on the thermal decomposition behavior of AN-based composite solid propellant. Part. Sci. Technol. **39**, 1–9 (2021)
6. M.K. Bharti, S. Gupta, S. Chalia, I. Garg, P. Thakur, A. Thakur, Potential of magnetic nanoferrites in removal of heavy metals from contaminated water: mini review. J. Supercond. Novel Magn. **33**, 3651–3665 (2020)
7. J.H. Hankiewicz, J. Stoll, J. Stroud, J. Davidson, K. Livesey, K. Tvrdy, A. Roshko, S.E. Russek, K. Stupic, P. Bilski, Nano-sized ferrite particles for magnetic resonance imaging thermometry. J. Magn. Magn. Mater. **469**, 550–557 (2019)
8. R. Verma, A. Chauhan, R. Kalia, K. M. Batoo and R. Kumar, Magnetic nanoferrites as an alternative for magnetic resonance imaging application. *Magnetic Nanoferrites and their Composites* (Elsevier) 237–56 (2023)
9. K. Malaie, M.R. Ganjali, Spinel nano-ferrites for aqueous supercapacitors; linking abundant resources and low-cost processes for sustainable energy storage. J Energy Storage **33**, 102097 (2021)
10. M.N. Akhtar, M. Yousaf, Y. Lu, M.A. Khan, A. Sarosh, M. Arshad, M. Niamat, M. Farhan, A. Ahmad, M.U. Khallidoon, Physical, structural, conductive and magneto-optical properties of rare earths (Yb, Gd) doped Ni–Zn spinel nanoferrites for data and energy storage devices. Ceramics Int. **47**, 11878–11886 (2021)
11. R. Kershi, Spectroscopic, elastic, magnetic and optical studies of nanocrystallite and nanoferro-fluids Co ferrites towards optoelectronic applications. Mater. Chem. Phys. **248**, 122941 (2020)
12. V.L.S. Vatsalya, G.S. Sundari, C.S. Sridhar, I.L. Prasanna, C.S. Lakshmi, Studies on nano crystalline copper doped Nickel Zinc ferrites for optoelectronic applications. J. Lumin. **252**, 119314 (2022)
13. M.K. Bharti, S. Chalia, P. Thakur, S. Sridhara, A. Thakur, P. Sharma, Nanoferrites heterogeneous catalysts for biodiesel production from soybean and canola oil: a review. Environ. Chem. Lett. **19**, 3727–3746 (2021)
14. S. Rana, A. Gallo, R. Srivastava, R. Misra, On the suitability of nanocrystalline ferrites as a magnetic carrier for drug delivery: functionalization, conjugation and drug release kinetics. Acta Biomater. **3**, 233–242 (2007)
15. S. Gautam, V. Thakur and N. Goyal, Nanoferrites as drug carriers in targeted drug delivery applications. *Applications of Nanostructured Ferrites* (Elsevier) pp. 161–178 (2023)
16. C.R. Vestal, Z.J. Zhang, Normal micelle synthesis and characterization of $MgAl_2O_4$ spinel nanoparticles. J. Solid State Chem. **175**, 59–62 (2003)
17. M.A. Baqiya, A. Taufiq, A.K. Sunaryono, M. Zainuri, S. Pratapa, D. Triwikantoro, *Spinel-structured nanoparticles for magnetic and mechanical applications. Magnetic Spinels-Synthesis, Properties and Applications* (Intech Open, London, 2017), pp.253–272
18. A. Omri, M. Bejar, E. Dhahri, M. Es-Souni, M. Valente, M. Graça, L. Costa, Electrical conductivity and dielectric analysis of $La_{0.75}$ (Ca, Sr)$_{0.25}$ $Mn_{0.85}Ga_{0.15}O_3$ perovskite compound. J. Alloys Compd. **536**, 173–178 (2012)
19. W.A.I. Tabaza, Synthesis and characterization of $MgAl_2O_4$ and ($MgxZn_{1-x}$) Al_2O_4) mixed spinel phospors. Thesis, University of the Free State (2014)
20. K.S. Abedini, G. Mahmoudzadeh, S. Madani, S. Sepehr, S. Manie, S. Moradi, F. Gharib, S.A. Mehrdad, A.P. Abromand, Determination of magnetic properties of nano-size $CoFe_2O_4$ particles synthesized by combination of sol-gel auto-combustion and ultrasonic irradiation techniques. J. Theor. Appl. Phys. **2**, 1–4 (2010)
21. D. Erdem, N.S. Bingham, F.J. Heiligtag, N. Pilet, P. Warnicke, L.J. Heyderman, M. Niederberger, $CoFe_2O_4$ and $CoFe_2O_4$-SiO_2 nanoparticle thin films with perpendicular magnetic anisotropy for magnetic and magneto-optical applications. Adv. Function. Mater. **26**, 1954–1963 (2016)
22. S. Hcini, A. Omri, M. Boudard, M.L. Bouazizi, A. Dhahri, K. Touileb, Microstructural, magnetic and electrical properties of $Zn_{0.4}M_{0.3}Co_{0.3}Fe_2O_4$ (M= Ni and Cu) ferrites synthesized by sol–gel method. J. Mater. Sci. Mater. Electron. **29**, 6879–6891 (2018)
23. A. Omelyanchik, M. Salvador, F. D'orazio, V. Mameli, C. Cannas, D. Fiorani, A. Musinu, M. Rivas, V. Rodionova, G. Varvaro, Magnetocrystalline and surface anisotropy in $CoFe_2O_4$ nanoparticles. Nanomaterials **10**, 1288 (2020)
24. M. Khodaei, S.S. Ebrahimi, Y.J. Park, J.M. Ok, J.S. Kim, J. Son, S. Baik, Strong in-plane magnetic anisotropy in (111)-oriented $CoFe_2O_4$ thin film. J. Magn. Magn. Mater. **340**, 16–22 (2013)

25. K. Maaz, A. Mumtaz, S. Hasanain, A. Ceylan, Synthesis and magnetic properties of cobalt ferrite ($CoFe_2O_4$) nanoparticles prepared by wet chemical route. J. Magn. Magn. Mater. **308**, 289–295 (2007)
26. M. Anupama, N. Srinatha, S. Matteppanavar, B. Angadi, B. Sahoo, B. Rudraswamy, Effect of Zn substitution on the structural and magnetic properties of nanocrystalline $NiFe_2O_4$ ferrites. Ceramics Int. **44**, 4946–4954 (2018)
27. W. Chiu, S. Radiman, R. Abd-Shukor, M. Abdullah, P. Khiew, Tunable coercivity of $CoFe_2O_4$ nanoparticles via thermal annealing treatment. J. Alloys Compd. **459**, 291–297 (2008)
28. A. Hilczer, K. Kowalska, E. Markiewicz, A. Pietraszko, B. Andrzejewski, Dielectric and magnetic response of $SrFe_{12}O_{19}$–$CoFe_2O_4$ composites obtained by solid state reaction. Mater. Sci. Eng. B **207**, 47–55 (2016)
29. S. Hcini, A. Selmi, H. Rahmouni, A. Omri, M.L. Bouazizi, Structural, dielectric and complex impedance properties of $T_{0.6}Co_{0.4}Fe_2O_4$ (T= Ni, Mg) ferrite nanoparticles prepared by sol gel method. Ceramics Int. **43**, 2529–2536 (2017)
30. A. Franco and V. S. Zapf, High temperature magnetic properties of $Co_{1-x}Mg_xFe_2O_4$ nanoparticles prepared by forced hydrolysis method. J. Appl. Phys. **111** (2012)
31. M.A. Lumbantoruan, E. Suharyadi, Effect of Zn on dielectric properties of Co-$ZnFe_2O_4$ magnetic nanoparticles. Key Eng. Mater. **840**, 448–453 (2020)
32. M.M. El-Masry, R. Ramadan, Enhancing the properties of PVDF/MFe_2O_4; (M: Co–Zn and Cu–Zn) nanocomposite for the piezoelectric optronic applications. J. Mater. Sci. Mater. Electron. **33**, 15946–15963 (2022)
33. E.-M. Mai and R. Ramadan, Study of PVDF/(Co-$ZnFe_2O_4$ and Cu-$ZnFe_2O_4$) nanocomposite for the piezo-phototronics applications (2022)
34. G.V. Duong, R.S. Turtelli, W. Nunes, E. Schafler, N. Hanh, R. Grössinger, M. Knobel, Ultrafine $Co_{1-x}Zn_xFe_2O_4$ particles synthesized by hydrolysis: effect of thermal treatment and its relationship with magnetic properties. J. Non-Crystall. Solids **353**, 805–807 (2007)
35. R. Arulmurugan, B. Jeyadevan, G. Vaidyanathan, S. Sendhilnathan, Effect of zinc substitution on Co–Zn and Mn–Zn ferrite nanoparticles prepared by co-precipitation. J. Magn. Magn. Mater. **288**, 470–477 (2005)
36. M. Assel, A. Altarawneh, R. Ghazy, O.M. Hemeda, A.M.A. Henaish, M. Mostafa, Correlation between structural, cation distribution with dielectric spectra and magnetic properties for Co–Zn ferrite doped with La^{3+} ions. Ceramics Int. **49**, 14215–14224 (2023)
37. H.S. Mund, B.L. Ahuja, Structural and magnetic properties of Mg doped cobalt ferrite nano particles prepared by sol-gel method. Mater. Res. Bull. **85**, 228–233 (2017)
38. S. Mandal, S. Mukherjee, Magnetocaloric effect and critical behaviour in zinc doped cobalt ferrite nanoparticles. J. Solid State Chem. **323**, 124008 (2023)
39. H.S. Mund, S. Tiwari, J. Sahariya, M. Itou, Y. Sakurai, B.L. Ahuja, Investigation of orbital magnetization in inverse spinel cobalt ferrite using magnetic Compton scattering. J. Appl. Phys. **110**, 073914 (2011)
40. S. Dhaka, S. Kumar, K. Poonia, V. Singh, K. Dhaka, H.S. Mund, Effect of annealing temperature on structural and magnetic properties of nano-cobalt ferrite. J. Mater. Sci. Mater. Electron. **32**, 16392–16399 (2021)
41. N. Kaur, M. Kaur, Processing and application of ceramics. Proc. Appl. Ceram. **8**(3), 137–143 (2014)
42. L.B. Tahar, H. Basti, F. Herbst, L. Smiri, J. Quisefit, N. Yaacoub, J. Grenèche, S. Ammar, $Co_{1-x}Zn_xFe_2O_4$ ($0 \leq x \leq 1$) nanocrystalline solid solution prepared by the polyol method: characterization and magnetic properties. Mater. Res. Bull. **47**, 2590–1598 (2012)
43. Q. Lin, Y. He, J. Lin, F. Yang, L. Wang, J. Dong, Structural and magnetic studies of Mg substituted cobalt composite oxide catalyst $Co_{1-x}Mg_xFe_2O_4$. J. Magn. Magn. Mater. **469**, 89 (2019)
44. M. Chakrabarti, D. Sanyal, A. Chakrabarti, Preparation of $Zn_{(1-x)}Cd_xFe_2O_4$ ($x = 0.0, 0.1, 0.3, 0.5, 0.7$ and 1.0) ferrite samples and their characterization by Mössbauer and positron annihilation techniques. J. Phys. Condens. Matter **19**, 236210 (2007)
45. H. Sozeri, Z. Durmus, A. Baykal, Structural and magnetic properties of triethylene glycol stabilized $Zn_xCo_{1-x}Fe_2O_4$ nanoparticles. Mater. Res. Bull. **47**, 2442–2448 (2012)
46. A. López-Ortega, E. Lottini, C.J. Fernandez, C. Sangregorio, Exploring the magnetic properties of cobalt-ferrite nanoparticles for the development of a rare-earth-free permanent magnet. Chem. Mater. **27**, 4048–4056 (2015)
47. Y. Köseoğlu, F. Alan, M. Tan, R. Yilgin, M. Öztürk, Low temperature hydrothermal synthesis and characterization of Mn doped cobalt ferrite nanoparticles. Ceram. Int. **38**, 3625–3634 (2012)
48. M. Anwar, F. Ahmed, B.H. Koo, Enhanced relative cooling power of $Ni_{1-x}Zn_xFe_2O_4$ ($0.0 \leqslant x \leqslant 0.7$) ferrites. Acta Mater. **71**, 100–107 (2014)
49. A. Mahmood, M.F. Warsi, M.N. Ashiq, M. Ishaq, Substitution of La and Fe with Dy and Mn in multiferroic $La_{1-x}Dy_xFe_{1-y}Mn_yO_3$ nanocrystallites. J. Magn. Magn. Mater. **327**, 64–70 (2013)
50. A. Abdeen, O. Hemeda, E. Assem, M. El-Sehly, Structural, electrical and transport phenomena of Co ferrite substituted by Cd. J. Magn. Magn. Mater. **238**, 75–83 (2002)
51. M. Ahmed, H. Afify, I. El Zawawia, A. Azab, Novel structural and magnetic properties of Mg doped copper nanoferrites prepared by conventional and wet methods. J. Magn. Magn. Mater. **324**, 2199–2204 (2012)
52. S. Hcini, S. Zemni, A. Triki, H. Rahmouni, M. Boudard, Size mismatch, grain boundary and bandwidth effects on structural, magnetic and electrical properties of $Pr_{0.67}Ba_{0.33}MnO_3$ and $Pr_{0.67}Sr_{0.33}MnO_3$ perovskites. J. Alloys Compd. **509**, 1394–1400 (2011)
53. A. Monshi, M.R. Foroughi, M.R. Monshi, Modified Scherrer equation to estimate more accurately nano-crystallite size using XRD. World J Nano Sci. Eng. **2**, 154–160 (2012)
54. R. Das and S. Sarkar, Determination of intrinsic strain in poly (vinylpyrrolidone)-capped silver nano-hexapod using X-ray diffraction technique. Curr. Sci. 775–778 (2015)
55. D. Balzar, H. Ledbetter, Voigt-function modeling in Fourier analysis of size-and strain-broadened X-ray diffraction peaks. J. Appl. Crystallogr. **26**, 97–103 (1993)
56. B. Warren, B. Averbach, The separation of cold-work distortion and particle size broadening in X-ray patterns. J. Appl. Phys. **23**, 497–497 (1952)
57. R. Jacob, J. Isac, X-ray diffraction line profile analysis of $BaSr_{0.6}Fe_{0.4}TiO_3$ [BSFTO]. Int. J. Chem. Stud. **2**, 12–21 (2015)
58. A. Omri, E. Dhahri, B.F.O. Costa, M.A. Valente, Structural, electric and dielectric properties of $Ni_{0.5}Zn_{0.5}FeCoO_4$ ferrite prepared by sol–gel. J. Magn. Magn. Mater. **499**, 166243 (2020)
59. A. Omri, E. Dhahri, B.F.O. Costa, M.A. Valente, Study of structural, morphological, Mössbauer and dielectric properties of $NiFeCoO_4$ prepared by a sol gel method. J. Sol-Gel Sci. Technol. **98**, 364–375 (2021)
60. M. Horchani, A. Omri, A. Benali, M.S. Eddine, A. Tozri, E. Dhahri, M. Graca, M. Valente, S. Jakka, B. Costa, Synthesis and investigation on the microstructural and electrical proprieties of $Ni_{0.1}Co_{0.5}Cu_{0.4}Fe_2O_4$ ferrite prepared using sol–gel route. J. Solid State Chem. **308**, 122898 (2022)
61. S.G. Pandya, J.P. Corbett, W.M. Jadwisienczak, M.E. Kordesch, Structural characterization and X-ray analysis by Williamson-Hall method for erbium doped aluminum nitride nanoparticles, synthesized using inert gas condensation technique. Physica E: Low-Dimension. Syst. Nanostruct. **79**, 98–102 (2016)

62. V. Mote, Y. Purushotham, B. Dole, Williamson-Hall analysis in estimation of lattice strain in nanometer-sized ZnO particles. J. Theor. Appl. Phys. **6**, 1–8 (2012)
63. G. Datt, M.S. Bishwas, M.M. Raja, A. Abhyankar, Observation of magnetic anomalies in one-step solvothermally synthesized nickel–cobalt ferrite nanoparticles. Nanoscale **8**, 5200–5213 (2016)
64. P. Chirawatkul, S. Khoonsap, S. Phumying, C. Kaewhan, S. Pinitsoontorn, S. Maensiri, Cation distribution and magnetic properties of $Co_xMg_{1-x}Fe_2O_4$ nanoparticles. J. Alloys Compd. **697**, 249–256 (2017)
65. T. Yu, Z. Shen, Y. Shi, J. Ding, Cation migration and magnetic ordering in spinel $CoFe_2O_4$ powder: micro-Raman scattering study. J. Phys. Condens. Matter **14**, L613 (2002)
66. W. Wang, Z. Ding, X. Zhao, S. Wu, F. Li, M. Yue, J.P. Liu, Microstructure and magnetic properties of MFe_2O_4 (M= Co, Ni, and Mn) ferrite nanocrystals prepared using colloid mill and hydrothermal method. J. Appl. Phys. **117**, 17A328 (2015)
67. F. Nekvapil, A. Bunge, T. Radu, S. Cinta Pinzaru, R. Turcu, Raman spectra tell us so much more: Raman features and saturation magnetization for efficient analysis of manganese zinc ferrite nanoparticles. J. Raman Spectrosc. **51**, 959–968 (2020)
68. R.S. Yadav, I. Kuřitka, J. Vilcakova, J. Havlica, J. Masilko, L. Kalina, J. Tkacz, J. Švec, V. Enev, M. Hajdúchová, Impact of grain size and structural changes on magnetic, dielectric, electrical, impedance and modulus spectroscopic characteristics of $CoFe_2O_4$ nanoparticles synthesized by honey mediated sol–gel combustion method. Adv. Nat. Sci.: Nanosci. Nanotechnol. **8**, 045002 (2017)
69. S. Singh, S. Munjal, N. Khare, Strain/defect induced enhanced coercivity in single domain $CoFe_2O_4$ nanoparticles. J. Magn. Magn. Mater. **386**, 69–73 (2015)
70. A. Benali, L. Saher, M. Bejar, E. Dhahri, M. Graca, M. Valente, P. Sanguino, L. Helguero, K. Bachari, A.M. Silva, Synthesis and physico-chemical characterization of Bi-doped Cobalt ferrite nanoparticles: cytotoxic effects against breast and prostate cancer cell lines. Eur. Phys. J. Plus **137**, 559 (2022)
71. G. Datt, A. Abhyankar, Dopant driven tunability of dielectric relaxation in MxCo (1–x) Fe_2O_4 (M: Zn2+, Mn2+, Ni2+) nanoferrites. J. Appl. Phys. (2017). https://doi.org/10.1063/1.4990275
72. S.M. Qaid, B. Al-Asbahi, H.M. Ghaithan, M. AlSalhi, Optical and structural properties of CsPbBr3 perovskite quantum dots/PFO polymer composite thin films. J. Colloid Interface Sci. **563**, 426–434 (2020)
73. D. Barreca, C. Massignan, S. Daolio, M. Fabrizio, C. Piccirillo, L. Armelao, E. Tondello, Composition and microstructure of cobalt oxide thin films obtained from a novel cobalt(II) precursor by chemicalvapor deposition. Chem. Mater. **13**, 588–593 (2001)
74. C.-S. Cheng, M. Serizawa, H. Sakata, T. Hirayama, Electrical conductivity of Co_3O_4 films prepared by chemical vapour deposition. Mater. Chem. Phys. **53**, 225–230 (1998)
75. M. Lenglet, C.K. Jørgensen, Reinvestigation of the optical properties of Co_3O_4. Chem. Phys. Lett. **229**, 616–620 (1994)
76. K.M.E. Miedzinska, B.R. Hollebone, J.G. Cook, An assigment of the optical absorption spectrum of mixed valence Co3O4 spinel films. J. Phys. Chem. Solids **48**, 649–656 (1987)
77. R. Mguedla, A.B.J. Kharrat, O. Taktak, H. Souissi, S. Kammoun, K. Khirouni, W. Boujelben, Experimental and theoretical investigations on optical properties of multiferroic $PrCrO_3$ ortho-chromite compound. Optic. Mater. **101**, 109742 (2020)
78. Gagandeep, K. Singh, B. Lark, H. Sahota, Attenuation measurements in solutions of some carbohydrates. Nuclear Sci. Eng. **134**, 208–217 (2000)
79. N.R. Dhineshbabu, V. Rajendran, N. Nithyavathy, R. Vetumperumal, Study of structural and optical properties of cupric oxide nanoparticles. Appl. Nanosci. **6**, 933–939 (2016)
80. M.A. Maksoud, G.S. El-Sayyad, A.M. El-Khawaga, M. Abd Elkodous, A. Abokhadra, M.A. Elsayed, M. Gobara, L. Soliman, H. El-Bahnasawy, A. Ashour, Nanostructured Mg substituted Mn-Zn ferrites: a magnetic recyclable catalyst for outstanding photocatalytic and antimicrobial potentials. J. Hazard. Mater. **399**, 123000 (2020)
81. A. Barhoumi, G. Leroy, B. Duponchel, J. Gest, L. Yang, N. Waldhoff, S. Guermazi, Aluminum doped ZnO thin films deposited by direct current sputtering: structural and optical properties. Superlattices Microstruct. **82**, 483–498 (2015)
82. G. Cody, Urbach edge of crystalline and amorphous silicon: a personal review. J. Non-crystall. Solids **141**, 3–15 (1992)
83. S. Husain, A.O. Keelani, W. Khan, Influence of Mn substitution on morphological, thermal and optical properties of nanocrystalline $GdFeO_3$ orthoferrite. Nano-Struct. Nano-Objects **15**, 17–27 (2018)
84. P. Petrik, N. Kumar, G. Juhasz, C. Major, B. Fodor, E. Agocs, T. Lohner, S.F. Pereira, H.P. Urbach, M. Fried, Optical characterization of macro-, micro- and nanostructures using polarized light. J. Phys. Conf. Ser. **558**, 012008 (2014)
85. P. Petrik, E. Agocs, J. Volk, I. Lukacs, B. Fodor, P. Kozma, T. Lohner, S. Oh, Y. Wakayama, T. Nagata, M. Fried, Resolving lateral and vertical structures by ellipsometry using wavelength range scan. Thin Solid Films **571**, 579–583 (2014)
86. B. Fodor, E. Agocs, B. Bardet, T. Defforge, F. Cayrel, D. Alquier, M. Fried, G. Gautier, P. Petrik, Porosity and thickness characterization of porous Si and oxidized porous Si layers—an ultraviolet–visible–mid infrared ellipsometry study. Microporous Mesoporous Mater. **227**, 112–120 (2016)
87. N. Tounsi, A. Barhoumi, F.C. Akkari, M. Kanzari, H. Guermazi, S. Guermazi, Structural and optical characterization of copper oxide composite thin films elaborated by GLAD technique. Vacuum **121**, 9–17 (2015)